



# Study of ZrS<sub>3</sub>-based field-effect transistors toward the understanding of the mechanisms of light-enhanced gas sensing by transition metal trichalcogenides

Katarzyna Drozdowska<sup>a,\*</sup>, Adil Rehman<sup>b</sup>, Sergey Rumyantsev<sup>b</sup>, Michelle Wurch<sup>c</sup>,  
Ludwig Bartels<sup>c</sup>, Alexander Balandin<sup>d</sup>, Janusz Smulko<sup>a</sup>, Grzegorz Cywiński<sup>b</sup>

<sup>a</sup> Department of Metrology and Optoelectronics, Faculty of Electronics, Telecommunications, and Informatics, Gdańsk University of Technology, G. Narutowicza 11/12, 80-233 Gdańsk, Poland

<sup>b</sup> CENTERA Laboratories, Institute of High Pressure Physics PAS, Warsaw, Poland

<sup>c</sup> Department of Chemistry, University of California, Riverside, CA 92521, USA

<sup>d</sup> Department of Electrical and Computer Engineering, University of California, Riverside, CA 92521, USA

## ARTICLE INFO

### Keywords:

Zirconium trisulfide  
ZrS<sub>3</sub>  
Transition metal trichalcogenides  
Gas sensor  
Light-enhanced sensing  
Visible light

## ABSTRACT

Extending knowledge of the properties of low-dimensional van der Waals materials, including their reactivity to the ambience, is important for developing innovative electronic and optoelectronic devices. Transition metal trichalcogenides with tunable optical band gaps and anisotropic conductivity are an emerging class among low-dimensional structures with the possibility of gate tunability and photoreactivity. These properties can be combined into light-enhanced field-effect transistor gas sensors. We demonstrated prototype zirconium trisulfide (ZrS<sub>3</sub>) sensors for nitrogen dioxide, ethanol, and acetone. Photoconductivity and photogating play a critical role in photoinduced gas sensing, with the dominance of the first for blue (470 nm) and green (515 nm) and the second one prevailing for red (700 nm) irradiations. Our results suggest that surface trap states lead both to trapping and scattering of the charge carriers in the channel. The gas detection is guided by charge transfer and modulation of the carrier mobility, resulting in distinct *I-V* characteristics for selected irradiation conditions.

## 1. Introduction

Since the discovery of graphene and its potential for applications in electronic devices, the research interest in exploring various two-dimensional (2D) materials has grown enormously [1,2]. The exceptional physical and chemical properties of graphene led to the development of carbon-based components in electronic devices, including anodes in batteries and cells, supercapacitors, flexible electronics, and different types of sensors and biosensors [3–5]. The following isolation of 2D transition metal dichalcogenides (TMDCs) opened a new route of using semiconducting monolayers with the possibility of the enhanced light-matter interaction owing to the tunable optical band gaps of TMDCs – an advantage compared to zero-band gap graphene [6–8]. Low-dimensional materials, including graphene and its derivatives, carbon nanotubes, polymer nanostructures, MXenes, TMDCs, nanostructured metal oxides (MOx), and their hybrids, are widely investigated for gas sensing applications. They are reviewed in many works

from the last three years, including different fabrication routes and sensing methodologies [9–15]. A relatively new class among low-dimensional structures are transition metal trichalcogenides (TMTCs) with general structural formula MX<sub>3</sub>, where M is a transition metal from group IVB (Ti, Zr, Hf) or group VB (Nb, Ta), and X is a chalcogen atom from group VIA (S, Se, Te) [16–19]. Similar to graphene or TMDCs, TMTC monolayers can be fabricated *via* chemical or mechanical exfoliation (top-down techniques) or through chemical vapor deposition (CVD) or chemical vapor transport (CVT) (bottom-up approaches). A recent report suggests an even more straightforward route of fabrication by printing from ink solutions, which was successfully realized for TiS<sub>3</sub> dispersed in the mixture of ethanol and ethylene glycol [20].

The layered structure of TMTCs exhibits in-plane solid anisotropy (e. g., in conducting properties) and quasi-one-dimensional (quasi-1D) electronic properties [20,21]. Moreover, quasi-1D structures are expected to exhibit interesting properties due to quantum confinement,

\* Corresponding author.

E-mail address: [katarzyna.drozdowska@pg.edu.pl](mailto:katarzyna.drozdowska@pg.edu.pl) (K. Drozdowska).

<https://doi.org/10.1016/j.mtcomm.2023.105379>

Received 8 December 2022; Received in revised form 3 January 2023; Accepted 9 January 2023

Available online 11 January 2023

2352-4928/© 2023 The Authors. Published by Elsevier Ltd. This is an open access article under the CC BY license (<http://creativecommons.org/licenses/by/4.0/>).

such as electron correlation, spin-orbit coupling, charge density wave phenomenon, and superconductivity [22,23]. Thus, the exceptional properties of TMTCs highlight their potential in a wide range of application fields, including field-effect transistors (FETs), photodetectors, photocatalysts, Li- & Na-ion batteries, thermoelectric materials, and sensors [24]. Studies of  $\text{MX}_3$  ( $\text{M} = \text{Ti}, \text{Zr}; \text{X} = \text{S}, \text{Se}$ ) band gaps by first-principle methods revealed an indirect band gap in the range of 0.21–1.83 eV and a direct band gap in the range of 0.73–2.13 eV in the bulk, meaning these materials should effectively absorb visible to infrared radiation [25]. For instance, quasi-1D  $\text{TiS}_3$  with  $\sim 1$  eV band gap may constitute an alternative to silicon in miniaturized electronics (the band gap of Si is  $\sim 1.17$  eV) [24,26].

Among other less-studied TMTCs, zirconium trisulfide ( $\text{ZrS}_3$ ) is a  $p$ -type semiconductor with a resistivity of  $15 \Omega\text{-cm}$  at room temperature in the bulk. However, nanostructured  $\text{ZrS}_3$  exhibited  $n$ -type semiconducting behavior [14,27]. Theoretical investigations revealed that  $\text{ZrS}_3$  possesses a wide direct band gap of 2.13 eV and an indirect band gap of 1.83 eV as a monolayer, offering the potential for effective visible light absorption [28].  $\text{ZrS}_3$  single crystals were reported to be efficient photodetectors with anisotropic photoresponse proportional to white light optical power at a temperature range of 100–300 K [25]. The same group demonstrated a wavelength-dependent photoresponse of  $\text{ZrS}_3$  crystals with the highest responsivity to blue light of 470 nm, compared to green (540 nm) and red (670 nm) irradiation [29]. The anisotropy in the electronic properties has been experimentally investigated for  $\text{ZrS}_3$  and  $\text{TiS}_3$  [30]. Moreover, it was reported that an exfoliated solid solution of  $\text{TiS}_3$  and  $\text{ZrS}_3$  has the potential to be used as FETs sensitive to visible light with a tunable optical band gap dependent on the Ti/Zr ratio [31].

Even though TMTCs incorporated in FETs and photodetectors were studied separately, no reports on combining these two applications into light-enhanced gas sensing devices based on quasi-1D  $\text{ZrS}_3$  were reported to the best knowledge of the authors. The ambient effect was studied for  $\text{ZrS}_3$  nanobelts, comparing the current-voltage characteristics in the dark and under selected irradiation for ambient air and vacuum conditions. A few times higher current was observed for the  $\text{ZrS}_3$  thin films under vacuum, and this effect was magnified under irradiation (405 nm) [32]. Interestingly, the opposite effect was observed for  $\text{ZrS}_3$  nanobelts fabricated *via* the reaction of zirconium and sulfur powders to form  $p$ -type semiconductors. The authors claim that the fabrication procedure influences the type of conductivity of  $\text{ZrS}_3$  films, which may result in different effects of ambient gases [33]. For  $p$ -type  $\text{ZrS}_3$ , oxygen molecules in the ambient air are adsorbed onto the nanobelt surface, capturing free electrons from the material to form  $\text{O}_2^-$  ions. This increases the hole concentration and amplifies the current when  $\text{ZrS}_3$  is a  $p$ -type semiconductor. These observations suggest that TMTCs may be responsive toward other gases, with the detection mechanisms presumably guided by charge transfer.

Although there is a lack of reports on  $\text{ZrS}_3$ -based gas sensors, the gas responsivity of  $\text{TaS}_3$  and  $\text{TiS}_3$  was demonstrated.  $\text{TaS}_3$  sensors showed selectivity toward NO compared to  $\text{H}_2\text{O}$ ,  $\text{N}_2$ ,  $\text{CO}_2$ , and  $\text{C}_6\text{H}_6$  [34]. Another work reported graphene/ $\text{TiS}_3$  heterojunctions investigated toward ethanol sensing [35]. Concentrations of ethanol between 2 and 20 ppm were efficiently detected at room temperature with 55% of relative humidity (RH). The authors observed that the sensor selectively detects polar vapors owing to the molecules' presence of  $-\text{OH}$  groups. Such a conclusion was suggested after watching much higher sensor responses toward ethanol, methanol, and acetone than small molecules such as  $\text{H}_2$ ,  $\text{CH}_4$ , and  $\text{CO}$ . Additionally, the authors suggested cleaning the sensor surface at  $170^\circ\text{C}$  in an argon environment after several cycles of detection to enable full recovery and higher sensing performance, showing the possibility of reversible sensing operation.

Here, we demonstrate a quasi-1D  $\text{ZrS}_3$ -based sensor offering quantitative detection of nitrogen dioxide ( $\text{NO}_2$ ), ethanol ( $\text{C}_2\text{H}_6\text{O}$ ), and acetone ( $\text{C}_3\text{H}_6\text{O}$ ) enhanced by visible light. We propose a FET configuration of the sensing device, where  $\text{ZrS}_3$  film acts as the channel. The possibility of gate voltage tuning enables channel conductivity

modulation to obtain higher sensing responses than in purely DC measurements. Blue (470 nm), green (515 nm), and red (700 nm) LEDs were used for light-enhanced detection to show the influence of wavelength and optical power density on  $\text{ZrS}_3$  sensor performance. Our work demonstrates  $\text{ZrS}_3$  sensor performance toward selected gases *via* transfer curves and time response measurements. We discuss possible gas sensing mechanisms supporting our considerations with channel current and conductivity studies of light-enhanced sensing. Our work discusses the mechanisms underlying the sensing process of nanostructured  $\text{ZrS}_3$  by comparing it to sensing properties exhibited by other 2D metal sulfides. We present a comprehensive study on possible modulation for  $\text{ZrS}_3$  sensor performance enhanced by FET configuration and optical tuning by selecting LED enhancement of specific wavelength and irradiance power.

## 2. Materials and methods

### 2.1. $\text{ZrS}_3$ sensors fabrication

The  $\text{ZrS}_3$  layers were mechanically exfoliated from the crystals produced by the chemical vapor transport (CVT) method using metallic zirconium and sulfur vapor in a vacuum-sealed quartz tube (2D Semiconductors). Details of the standard CVT methods are well described in the literature for TMDC and TMTC materials [30,36]. A thin film consisting of  $\text{ZrS}_3$  nanowires (quasi 1D nanoribbons) served as a channel in field effect transistors (FETs). Golden electrodes (source and drain) were deposited to obtain  $\text{ZrS}_3$  channels of width and length equal to  $2 \mu\text{m}$  and  $1.5 \mu\text{m}$ , respectively. Si substrate served as a back-gate contact in  $\text{ZrS}_3$  FET.

### 2.2. DC characteristics measurements

DC response measurements were performed in a probe station using titanium needles to connect the  $\text{ZrS}_3$  sensor's electrodes with the measuring and biasing units. A Keithley-4200A-SCS parameter analyzer with two medium power source-measure units (type 4201-SMU) was used for the transfer and output characteristics measurements and time-domain studies. All drain-source current vs. gate voltage curves ( $I_{\text{DS}}-V_{\text{G}}$ ) were collected in the  $V_{\text{G}}$  range from  $-30$  to  $+30$  V with a  $0.1$  V step and  $2$  s hold time. The drain-source voltage ( $V_{\text{DS}}$ ) was kept equal to  $6$  V. Output characteristics ( $I_{\text{DS}}-V_{\text{DS}}$ ) were collected in the  $V_{\text{DS}}$  range from  $-5$  to  $+10$  V.  $V_{\text{G}}$  was limited to  $30$  V. Time-domain studies were performed at  $V_{\text{DS}} = 6$  V and  $V_{\text{G}} = 30$  V since the sensing responses were the most pronounced for the high positive gate voltage. During all measurements, the sensor was kept inside a metal box to limit interference by ambient light, power supply lines, and laboratory airflow during gas-sensing experiments. Light-assisted sensing was realized using three LEDs in the visible light range: blue ( $\lambda = 470$  nm), green ( $\lambda = 515$  nm), and red ( $\lambda = 700$  nm). The LEDs were positioned approximately  $0.5$  cm from the sensor surface to obtain relatively high optical power densities, estimated as  $1.44$   $\text{mW}/\text{cm}^2$ ,  $4.05$   $\text{mW}/\text{cm}^2$ , and  $0.91$   $\text{mW}/\text{cm}^2$  for blue, green, and red LEDs, respectively. Three blue LEDs (470 nm) were positioned at a fixed distance ( $\sim 0.5$  cm) from the sensing surface to investigate the impact of different optical powers at a fixed wavelength. The diode current was changed between  $5$  mA and  $30$  mA, which increased the optical power density from  $0.93$   $\text{mW}/\text{cm}^2$  to  $4.30$   $\text{mW}/\text{cm}^2$ . For more details on the types of LEDs used in our experiments and their optical properties, see Table A.1 in [Supplementary Material](#).

### 2.3. Gas-sensing experiments

A metal pipe connected to the gas distribution system was placed within  $0.5$  cm from the sensor surface to transport selected target gases. Nitrogen dioxide ( $\text{NO}_2$ ), ethanol ( $\text{C}_2\text{H}_6\text{O}$ ), and acetone ( $\text{C}_3\text{H}_6\text{O}$ ) gases were used for sensing experiments (all diluted in  $\text{N}_2$ ). Dry synthetic air (S.A.) was used as a reference gas and to obtain selected concentrations

of target gases by mixing them with S.A. at specific proportions. During all gas sensing measurements, we kept a constant overall gas flow of 50 mL/min regulated by mass flow controllers (Analyt-MTC, model GFC17). Three gases were selected for sensing experiments using a quasi-1D ZrS<sub>3</sub> sensor. We chose nitrogen dioxide (NO<sub>2</sub>), one of the toxic gases harmful to both humans and the environment, even at low concentrations, as a representative inorganic gas [37]. In addition, we selected two organic gases: ethanol (C<sub>2</sub>H<sub>6</sub>O) and acetone (C<sub>3</sub>H<sub>6</sub>O) vapors, to test the sensor's selectivity by utilizing DC measurements. Both ethanol and acetone are substances that, if present in an exhaled breath at specific concentrations, can provide crucial information for health monitoring and medical diagnosis [38–40]. The DC characteristics were collected after stabilizing the sensor response in the selected environment/irradiation conditions for ~10 min. All experiments were conducted at room temperature (RT ~23 °C) and ambient pressure (~1 bar).

### 3. Results and discussion

We investigated the ZrS<sub>3</sub>-based sensor fabricated in a FET configuration according to the scheme provided in Fig. 1a. For all gas sensing experiments, the length and width of the FET channel amounted to 1.5 μm and 2 μm, respectively, yielding 3 μm<sup>2</sup> of a sensor's active area (Fig. 1b). Fig. 1c and Fig. 1d present the reference and output characteristics of the ZrS<sub>3</sub>-based FET sensor in the reference atmosphere of S.A. in the dark and under selected LEDs from the visible light spectral range. Both characteristics indicate that the ZrS<sub>3</sub> layer exhibits *n*-type semiconducting behavior. Fig. 1c shows a wide hysteresis, which is more pronounced for blue and green irradiation than for red light and dark conditions. Applied irradiation induces photocurrent in the layer, increasing the overall current flowing through the ZrS<sub>3</sub> channel. As

nanostructured ZrS<sub>3</sub> was reported to have an optical bandgap of ~1.8–1.9 eV, the structure should efficiently absorb wavelengths below ~690 nm. The longer wavelengths may be absorbed if any discrete defect levels are present below the conduction band, which can be observed for the defective or doped semiconductors. Thus, one can see that the red light (0.91 mW/cm<sup>2</sup> of optical power density) has the lowest impact on the I<sub>DS</sub> compared to the blue and green irradiation, presumably owing to the mid-gap energy levels in ZrS<sub>3</sub>. Interestingly, the green light increases the current the most. It confirms that ZrS<sub>3</sub> response to irradiation depends on both wavelength and optical power of the light source, as the optical power density for the green LED exceeded the value for the blue LED almost three times (1.44 mW/cm<sup>2</sup> and 4.05 mW/cm<sup>2</sup> for blue and green LED, respectively).

Fig. 2 depicts I<sub>DS</sub>-V<sub>G</sub> characteristics of the ZrS<sub>3</sub> sensor toward different concentrations of NO<sub>2</sub> (4–16 ppm) in four cases of light enhancement: in the dark, under red (700 nm), green (515 nm), and blue (470 nm) irradiation. In all cases, the curves shift downwards – the current decrease means the sensing layer increases its resistance, which confirms the oxidizing ability of NO<sub>2</sub> molecules for *n*-type ZrS<sub>3</sub>. As seen from Figs. 2c and 2d, blue and green irradiation increases I<sub>DS</sub> noticeably, magnifying the hysteresis and stabilizing the sensor response, which can be more vulnerable to current fluctuations at the level of a few nA (dark and red-light case). Thus, blue or green light enhancement is suggested for providing conditions that enable a more stable and easily measurable response (at tens or hundreds of nA) and facilitate room-temperature sensor operation. Analogous sensing experiments were conducted for 30–90 ppm of ethanol and 20–35 ppm of acetone (Figs. A.1 and A.2). In contrast with NO<sub>2</sub>, both organic gases increased I<sub>DS</sub> (equally decreased sensor resistance), suggesting their reducing character toward the ZrS<sub>3</sub> layer. Such direction of changes induced in the sensor was reported before for ethanol and acetone detection by TiS<sub>3</sub> flakes deposited as a

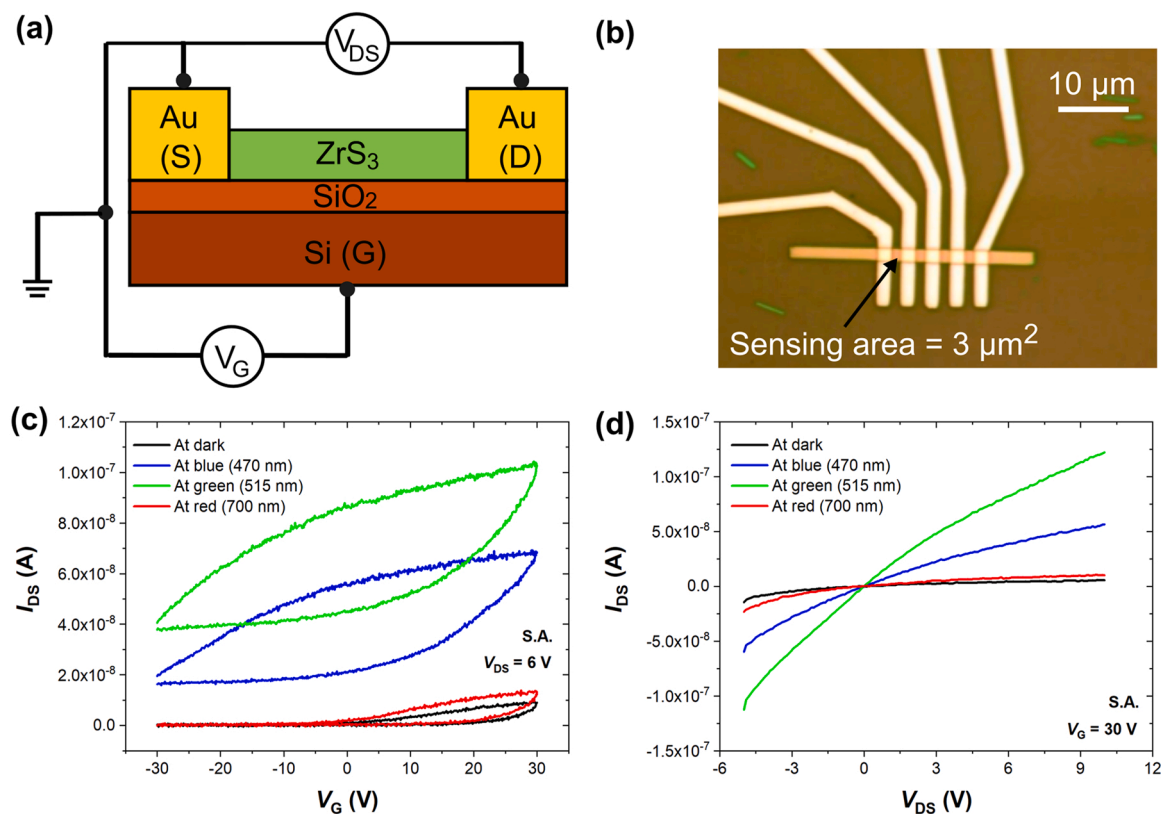
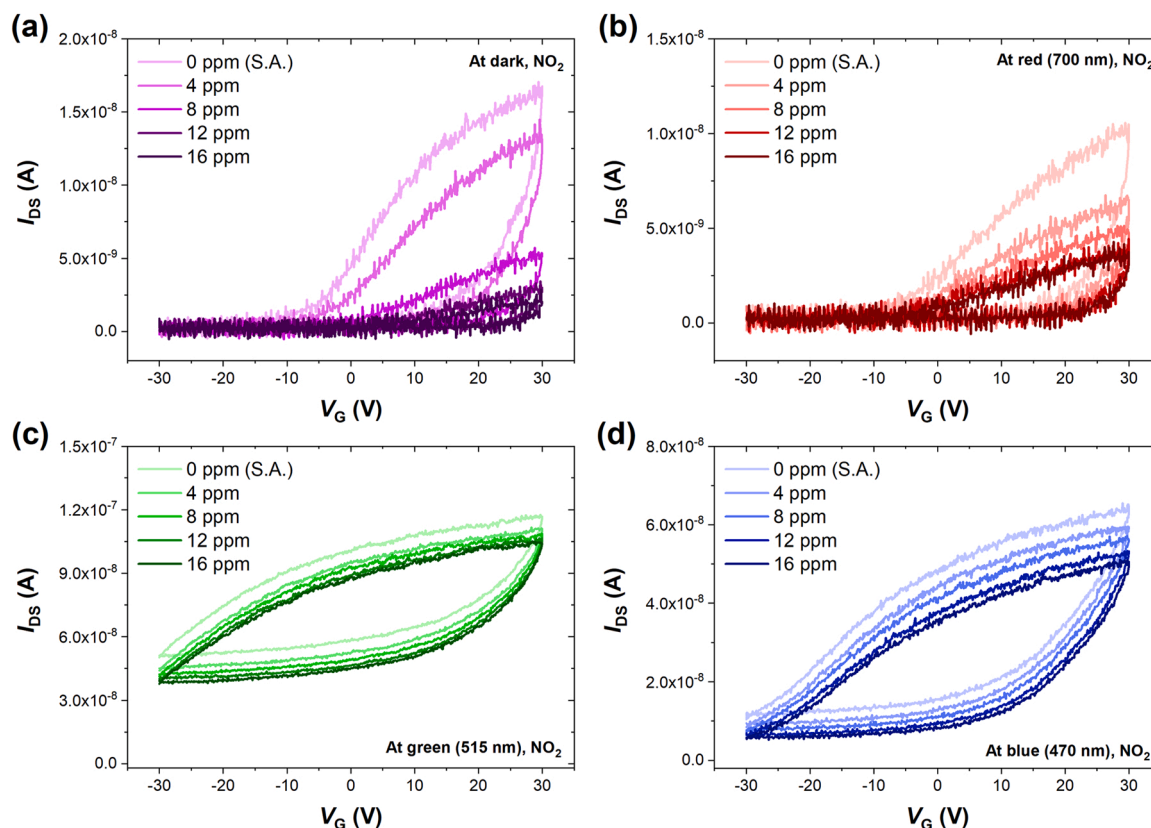


Fig. 1. (a) Schematic representation of the ZrS<sub>3</sub>-based sensor, and (b) microscopic photograph of the investigated sensing structure with a 3 μm<sup>2</sup> sensing area between each pair of electrodes. Reference DC measurements of the ZrS<sub>3</sub> FET sensor in synthetic air (S.A.): (c) transfer curve (drain-source current I<sub>DS</sub> as a function of gate voltage V<sub>G</sub>) with drain-source voltage V<sub>DS</sub> biased to 6 V, and (d) output curve (I<sub>DS</sub> vs. V<sub>DS</sub>) with V<sub>G</sub> biased to 30 V in the dark and under blue (470 nm, 1.44 mW/cm<sup>2</sup>), green (515 nm, 4.05 mW/cm<sup>2</sup>), and red (700 nm, 0.91 mW/cm<sup>2</sup>) irradiation.



**Fig. 2.** ZrS<sub>3</sub> sensor performance toward selected concentrations of NO<sub>2</sub> under different irradiation conditions: graphs (a)–(d) present drain-source current  $I_{DS}$  vs. gate voltage  $V_G$  for NO<sub>2</sub> detection in the dark and under red (700 nm, 0.91 mW/cm<sup>2</sup>) green (515 nm, 4.05 mW/cm<sup>2</sup>), and blue (470 nm, 1.44 mW/cm<sup>2</sup>) light, respectively.

channel between Au electrodes [35]. Moreover, similarly to the NO<sub>2</sub> case, blue and green irradiation stabilize sensor responses toward ethanol and acetone. To address the selectivity of the sensor, we compared the sensor response to the same concentration of ethanol and acetone (30 ppm). The relative change of  $I_{DS}$  (the sensor response) under green irradiation is  $\sim 4.7\%$  for 30 ppm of ethanol and  $\sim 9.2\%$  for 30 ppm of acetone. The difference in values for the blue light case is even more apparent, estimated as  $\sim 2.8\%$  and  $\sim 14\%$  for 30 ppm of ethanol and acetone, respectively. Such observations suggest a higher affinity between acetone molecules and ZrS<sub>3</sub> structure than for ethanol molecules.

Fig. 3 summarizes  $I_{DS}$  changes for selected nitrogen dioxide, ethanol, and acetone concentrations.  $I_{DS}$  values were derived from corresponding  $I_{DS}$ - $V_G$  characteristics for  $V_G = 30$  V. Dashed lines designate the linear fit functions, with  $R^2$  values indicating the quality of the linear fitting. The  $R^2$  coefficient represents how well the linear model predicts the experimental data, and  $R^2$  values close to 1 show the high linearity of the gas-sensing responses. In the case of NO<sub>2</sub>, high linearity in sensor response was observed for blue and green irradiation. For ethanol and acetone, all types of irradiation and dark conditions resulted in similarly high linearity of the sensor response. The opposite direction of  $I_{DS}$  changes for inorganic NO<sub>2</sub> and organic ethanol and acetone can be explained by each molecule's acceptor or donor properties. Generally, the gas detection mechanism for two-dimensional metal sulfides relies primarily on charge transfer between the sensing material and analyte, as reported for nanostructured MoS<sub>2</sub> – the leading representative of the 2D materials with tunable band gaps [14]. The amount of charge donated or extracted from the material by the adsorbed molecules affects the electron carrier density of the semiconducting layer, altering its resistance. Additionally, the FET configuration of the sensor modulates the electric field across the dielectric layer, influencing the channel conductivity.

Apart from that, two main effects were suggested to explain the

changes in  $I$ - $V$  characteristics for light-activated FETs consisting of low-dimensional structures. The first, photoconductive effect, results in the induced photocurrent in the channel due to generated charge carriers during irradiation; the second, photogating (photovoltaic) effect, leads to a change in FET threshold voltage, shifting the  $I$ - $V$  sideways [41,42]. For visible light-enhanced MoS<sub>2</sub>-based sensors, the dominant photogating effect was demonstrated, which resulted in a negative shift of FET threshold voltage  $V_{th}$  for increased irradiation [43]. However, according to the standard charge transfer model of gas detection for metal sulfides, electrons extracted from the sensing material during NO<sub>2</sub> adsorption should shift  $V_{th}$  toward positive values without changing the shape ( $I$ - $V$  hysteresis slope) of the  $I_{DS}$ - $V_G$  curve. Since the channel conductivity depends on both carrier concentration and mobility, the changes introduced in both factors may alter the current flowing through the sensor. The abovementioned observations obtained for NO<sub>2</sub> sensing by MoS<sub>2</sub> were ascribed to the carrier mobility change induced by adsorbed target gas molecules acting as scattering centers for channel electrons. The scattering of electrons reduces their mobility resulting in the drain-source current decrease. At the same time, we cannot exclude the fact that adsorbed molecules may capture electrons during photoexcitation, limiting their concentration, which diminishes the channel current. In the case of our gas sensing results, the change of hysteresis shape is visible primarily for dark and red-light conditions, whereas for green and blue irradiation, the  $I_{DS}$  level increases one or two orders of magnitude, but the hysteresis shape is almost unaltered. This suggests that photoinduced charge carriers significantly increase channel current resulting in a positive photoconductivity, so the photoconductive effect play an essential role in the gas detection under blue and green light. At the same time, one can notice the simultaneous sideways shift and the change of hysteresis shape, especially for dark and red-light conditions. Thus, we conducted subsequent studies to develop more detailed

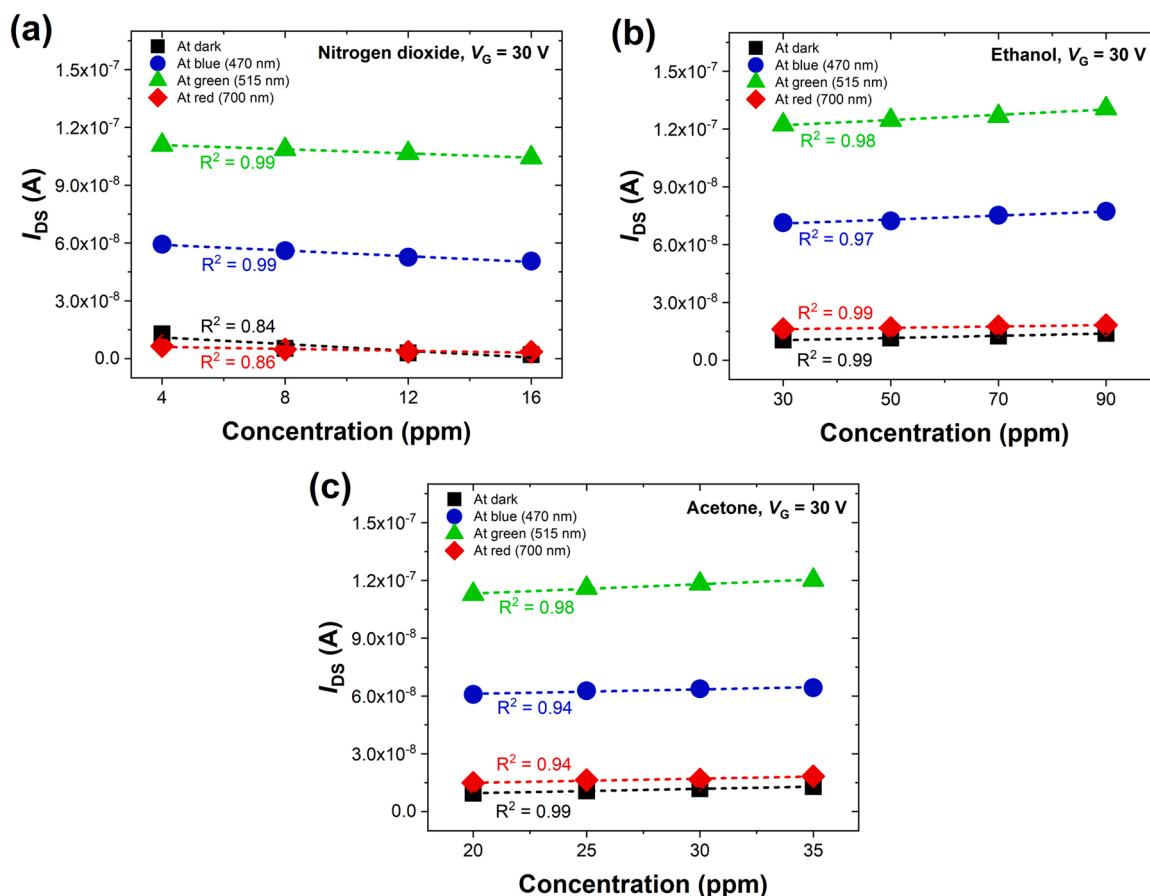


**Fig. 3.** Comparison of  $\text{ZrS}_3$  sensor performance toward different gases: drain-source current  $I_{DS}$  response for selected concentrations of (a) nitrogen dioxide ( $\text{NO}_2$ ), (b) ethanol, and (c) acetone under different irradiation conditions.  $I_{DS}$  values were taken for the  $V_G = 30$  V.  $V_{DS}$  was biased to 6 V in all experiments. Dashed lines depict linear functions fitted to the experimental points.

conclusions on  $\text{ZrS}_3$ -based gas sensing including the effect of electron concentration and mobility change and taking photoconductive and photogating effects into consideration.

As blue and green light enhanced the  $\text{ZrS}_3$  sensor response noticeably, we chose these two LEDs for further gas sensing experiments. Fig. 4a demonstrates time response studies of the  $\text{ZrS}_3$  sensor toward repeatable cycles of introducing 16 ppm of  $\text{NO}_2$  under green and blue irradiation. The transient curves were collected for  $V_{DS}$  and  $V_G$  biased to 6 V and 30 V, respectively. Again, we confirm that green light increases

$I_{DS}$  more significantly despite a longer wavelength, which can be ascribed to its higher optical power. To check whether optimizing the sensor response is possible by adjusting LED optical power, we used three blue LEDs (470 nm) connected in series to a voltage supplier for sensor irradiation to obtain a wider range of irradiance adjusted by the diodes' polarization current. Fig. 4b shows cycles of 16 ppm of  $\text{NO}_2$  introduction during irradiation with blue LEDs of selected optical power densities (marked on the graph with dashed boxes indicating periods for selected irradiation conditions). Increasing optical power densities in

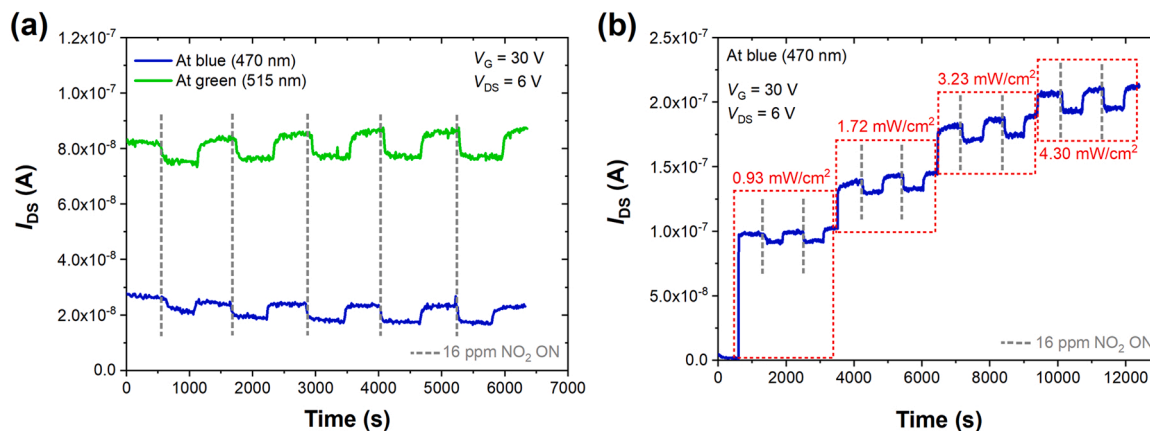


**Fig. 4.** Time response studies of the  $\text{ZrS}_3$  sensor for consecutive cycles of introducing 16 ppm of  $\text{NO}_2$  (a) under continuous irradiation using green (515 nm,  $4.05 \text{ mW}/\text{cm}^2$ ) or blue (470 nm,  $1.44 \text{ mW}/\text{cm}^2$ ) LED and (b) under continuous blue light (three LEDs) with adjusted optical power density from  $0.93 \text{ mW}/\text{cm}^2$  to  $4.30 \text{ mW}/\text{cm}^2$  (dashed boxes indicate cycles of  $\text{NO}_2$  detection for specific optical power densities with values marked in the figure).

the range of 0.93–4.30 mW/cm<sup>2</sup> led to rapid baseline current growth, and the overall increase of  $I_{DS}$  change during exposition to target gas. By examining different optical parameters of LEDs used in our studies, we can confirm that ZrS<sub>3</sub> sensor response toward NO<sub>2</sub> depends on the wavelength and optical power density, which provide different methods of ZrS<sub>3</sub> performance modulation for optimization of sensor operation in ambient conditions (room temperature and atmospheric pressure). Moreover, the average sensor response (the relative change of  $I_{DS}$  before and after exposition to NO<sub>2</sub>) did not vary much for increasing irradiance yielding 8.10%, 6.21%, 6.21%, and 7.12% for their optical radiation powers of 0.93 mW/cm<sup>2</sup>, 1.72 mW/cm<sup>2</sup>, 3.23 mW/cm<sup>2</sup>, and 4.30 mW/cm<sup>2</sup>, respectively. This observation suggests that different optical parameters of LEDs mainly affect the baseline current for measurement modulation but do not significantly influence the detection process. The constant or weak dependence between sensor response and irradiation power may imply carrier mobility modulation during light-enhanced sensing, according to [43], since in a purely charge-transfer mechanism, the sensor response should vary more significantly with increasing optical power density. However, comparing relative sensor responses between repeatable detection cycles for green and blue light, a significant difference between average responses can be observed, amounting to 26.12% for blue and 9.96% for green light. Here, an almost three times higher response for blue light-enhanced sensing stems from a significant difference in the current baseline and indicates that the photoconductive effect shifting DC characteristics upwards becomes a relevant factor when comparing LEDs of varying wavelengths and optical powers, and the sensor response should be normalized to compare the results reliably. Additionally, based on the time response studies, one could see the high stability of the sensor response both to green or blue irradiation and to 16 ppm of NO<sub>2</sub>. Despite the very low measured currents (maximum tens or hundreds of nA), the sensor baseline remains stable, indicating the short-time stability of the device with reduced short-time drift. We want to note that the sensor remained responsive to selected gases under lighting conditions for around two months of ongoing measurements, suggesting long-time stability of the sensing structure.

Undoubtedly, the photocurrent induced during sensor irradiation increases the overall  $I_{DS}$  noticeably while comparing dark and green conditions, as seen in Fig. 2 and Fig. 4a. Additional irradiation emphasizes the photoconductive effect due to a high number of generated excess carriers. However, as already mentioned, photoinduced carriers may be captured or scattered during gas adsorption. The trap centers may be present due to defects, adsorbents, or dopants and guide the photoconductive and photogating effect [44]. According to [42], the photogating effect arises from charge trapping occurring at the surface binding sites for monolayered MoS<sub>2</sub>. Thus, in different ambiances,  $V_{th}$  is likely to shift due to capturing or donating electrons by surface states to the target molecules adsorbed on the active material. In our studies, all three gases shift the  $I_{DS}$ - $V_G$  curve sideways noticeably for dark conditions and under weak red irradiation enhancement. In general, if the trap centers capture the electrons, the  $I_{DS}$ - $V_G$  curve shifts to the right, whereas if the trap centers capture the holes, the opposite effect with the shift to the left is observed. For the ZrS<sub>3</sub> sensor, the shift is positive for NO<sub>2</sub> but negative for ethanol and acetone (Figs. A.1, A.2), which agrees with the acceptor properties of NO<sub>2</sub> and donor properties of both organic gases. Moreover, the higher the gas concentration, the greater the  $V_{th}$  shift, making quantitative detection possible for the ZrS<sub>3</sub> sensor. The direction of the shift conforms with the charge transfer mechanism. However, the additional change of hysteresis shape implies that carrier mobility modulation also occurs during molecular detection, presumably due to the scattering of carriers. On the other hand, for gas sensing under blue and green irradiation, the shape of the transfer curves remains almost unaltered for different concentrations of all three gases, whereas the visible change in  $I_{DS}$  level occurs. Such results may indicate the dominant photoconductive effect responsible for detection processes in these irradiation conditions. For a specific wavelength range and

under sufficient irradiance, the capture and release of carriers by trap states guide the adsorption/desorption processes and dominate over scattering on surface defects and adsorbed molecules. On the other hand, without sufficient light enhancement (dark conditions or longer wavelengths), the lower number of charge carriers flowing through the channel may be more susceptible to scattering, which reduces their mobility making the photogating effect with a change of hysteresis shape dominant.

Furthermore, the dominance of the photoconductive effect for blue or green light-enhanced gas sensing (irradiation of shorter wavelengths) does not entirely exclude the impact of the photogating effect on NO<sub>2</sub> detection by quasi-1D ZrS<sub>3</sub> since the simultaneous occurrence of both phenomena is the most probable case. Therefore, we conducted additional measurements for various concentrations of NO<sub>2</sub> (2–16 ppm) under blue irradiation of the highest optical power density (4.30 mW/cm<sup>2</sup>). We transformed obtained results into sensor conductance response ( $S_G$ ) derived from  $I_{DS}$  values at  $V_G = 30$  V and  $V_{DS}$  biased to 6 V. We define  $S_G$  as a relative change of sensor conductance  $G$  in relation to sensor conductance  $G_0$  measured in the reference atmosphere of S.A. –  $|G - G_0|/G_0$ . It was previously reported for MoS<sub>2</sub> and reduced graphene oxide (rGO) that sensor response depends on gas concentration according to the Langmuir equation, revealing the saturation of the response for a specific concentration threshold [43,45]. In those cases, the sensor response relied on the surface coverage of target molecules on the adsorption sites, which eventually saturated. A similar effect is visible in Fig. 5a for NO<sub>2</sub> concentrations exceeding 8 ppm. The linear relationship between the inverse conductance response and concentration may imply that visible response changes are solely due to channel conductivity change, and any other effects are negligible. According to these considerations, the deviation from the linear dependence between  $1/S_G$  and  $1/Concentration$  in the case of the ZrS<sub>3</sub> sensor (Fig. 5b) suggests the coexistence of more than one process responsible for detection, which agrees with our previous assumptions.

#### 4. Conclusions

We investigated a FET-configured gas sensor based on quasi-1D ZrS<sub>3</sub> for qualitative and quantitative detection of nitrogen dioxide, ethanol, and acetone under ambient conditions. Our results show that light-activated ZrS<sub>3</sub> sensor performance can be easily optimized by adjusting the optical parameters of LEDs to ensure high sensitivity and stability of the sensor at room temperature while keeping low-power consumption of the device. This way, we demonstrate another material from the family of 2D metal-chalcogen compounds for light-enhanced gas sensing, proposing the possibility of sensing performance tunability with the FET configuration of the device and optimization of the photoactivation process.

Our gas sensing studies reveal the possibility of up to two orders of magnitude enhancement (from ~1 nA to hundreds of nA) of sensor channel current under green and blue irradiation with irradiances reaching ~4 mW/cm<sup>2</sup>. Such photoexcitation provides the current baseline less susceptible to random fluctuations and a more stabilized sensor response toward ambient gases. Even though the sensor does not exhibit an excellent selectivity to any of the investigated gases, the direction of  $I_{DS}$  changes enables the discrimination between NO<sub>2</sub> and organic gases due to their redox properties. Moreover, comparing the sensor response toward the same concentration of ethanol and acetone (30 ppm) supports distinguishing between these two organic gases (Figs. A.1 and A.2). Time-response studies confirmed the sensor stability and repeatability for 16 ppm of NO<sub>2</sub> detected under green and blue irradiation without short-time drift of channel current.

A few aspects should be considered in the discourse on gas sensing mechanisms by quasi-1D ZrS<sub>3</sub> presented in our work. First, the coexistence of photoconductive and photogating effect presumably guide the surface processes during the light-enhanced detection of selected gases. Depending on the external irradiation, mainly the optical parameters of

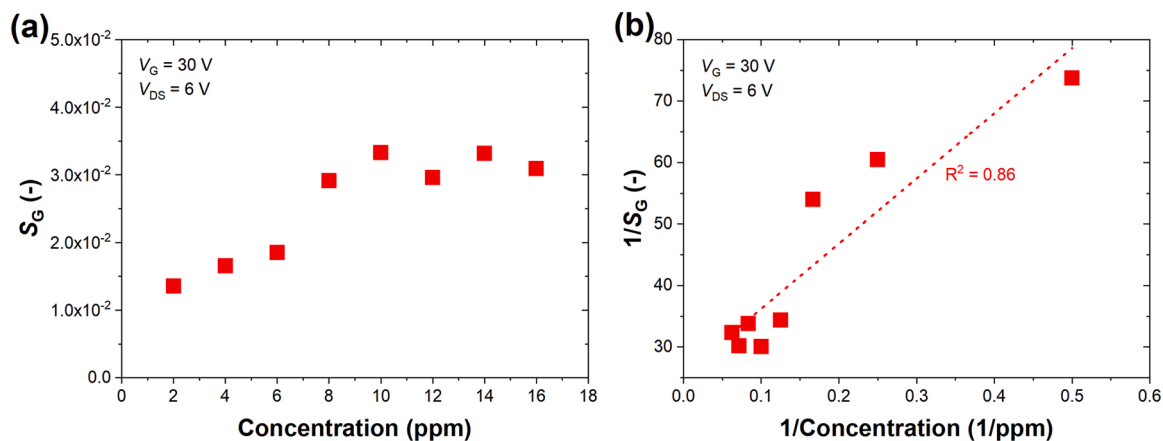


**Fig. 5.** (a) ZrS<sub>3</sub> sensor response derived from the relative changes of conductance  $S_G$  vs. NO<sub>2</sub> concentration (2–16 ppm), and (b) the inverse conductance response vs. the inverse NO<sub>2</sub> concentration. Conductivity values were derived from the transfer curves for  $V_G = 30$  V and  $V_{DS}$  biased to 6 V under blue irradiation of the highest optical power density (4.30 mW/cm<sup>2</sup>).

the used LEDs, one of these effects becomes dominant. Although there is no photoexcitation in the dark, the change in the threshold voltage still occurs due to the interaction of channel electrons with gas molecules acting as trapping and scattering centers after adsorption. For the red irradiation, the wavelength of the LED (700 nm) may be insufficient to excite electrons directly from the valence band to the conduction band, but in case of any discrete levels in the band gap (defect levels, mid-gaps), some excess carriers may participate in molecular detection with a high possibility of being scattered on the adsorbed molecules. For blue and green irradiation, the shorter wavelengths allow photoactivation of the material providing high photoconductive gain and the subtle shift of the threshold voltage of FET. The dominance of the photoconductive effect does not eliminate the photogating in this case; furthermore, the impact of the channel electrons scattered on the adsorbed molecules can be tentatively confirmed by (i) the change of hysteresis shape ( $I$ - $V$  hysteresis slope), (ii) low dependence between optical power and sensor response, and (iii) non-linear relationship between the inverse sensor conductance response and gas concentration.

Our findings shed light on light-driven gas sensing mechanisms by quasi-1D ZrS<sub>3</sub>, broadening the possibility of using transition metal trichalcogenides in electronic and optoelectronic real-environment applications. Our work also broadens the understanding of surface science among 2D materials in general, extending the range of 2D (quasi-1D) structures as potential candidates for optimized gas sensing.

#### CRediT authorship contribution statement

J.S. and S.R. conceived the study. K.D. established and ran the experimental electrical and optical studies, evaluated analysis, and proposed interpretation. A.R. and M.W. participated in the fabrication and characterization of the samples. L.B. supervised sample preparation. A.B. contributed to data analysis. K.D., J.S., S.R., and G.C. wrote the manuscript. All authors had an opportunity to edit the manuscript.

#### Declaration of Competing Interest

The authors declare that they have no known competing financial interests or personal relationships that could have appeared to influence the work reported in this paper.

#### Data availability

Data will be made available on request.

#### Acknowledgments

This work was funded by the National Science Centre, Poland, the research project: 2019/35/B/ST7/02370, “System of gas detection by two-dimensional materials”. This work was also partially supported by the “International Research Agendas” program of the Foundation for Polish Science, co-financed by the European Union under the European Regional Development Fund (No. MAB/2018/9). A.B. and L.B. acknowledge partial support from the National Science Foundation (NSF) program Designing Materials to Revolutionize and Engineer our Future (DMREF) via a project DMR-1921958.

#### Appendix A. Supporting information

Supplementary data associated with this article can be found in the online version at [doi:10.1016/j.mtcomm.2023.105379](https://doi.org/10.1016/j.mtcomm.2023.105379).

#### References

- [1] C. Anichini, W. Czepa, D. Pakulski, A. Aliprandi, A. Ciesielski, P. Samorì, Chemical sensing with 2D materials, *Chem. Soc. Rev.* 47 (2018) 4860–4908, <https://doi.org/10.1039/c8cs00417j>.
- [2] R. Vargas-Bernal, Electrical properties of two-dimensional materials used in gas sensors, *Sensors* 19 (2019) 1295, <https://doi.org/10.3390/s19061295>.
- [3] A. Nag, A. Mitra, S.C. Mukhopadhyay, Graphene and its sensor-based applications: a review, *Sens. Actuators A Phys.* 270 (2018) 177–194, <https://doi.org/10.1016/j.sna.2017.12.028>.
- [4] X. Huang, Z. Yin, S. Wu, X. Qi, Q. He, Q. Zhang, Q. Yan, F. Boey, H. Zhang, Graphene-based materials: synthesis, characterization, properties, and applications, *Small* 7 (2011) 1876–1902, <https://doi.org/10.1002/SMLL.2011002009>.
- [5] Y. Zhu, S. Murali, W. Cai, X. Li, J.W. Suk, J.R. Potts, R.S. Ruoff, Graphene and graphene oxide: synthesis, properties, and applications, *Adv. Mater.* 22 (2010) 3906–3924, <https://doi.org/10.1002/ADMA.201001068>.
- [6] E. Lee, Y.S. Yoon, D.J. Kim, Two-dimensional transition metal dichalcogenides and metal oxide hybrids for gas sensing, *ACS Sens.* 3 (2018) 2045–2060, <https://doi.org/10.1021/acssensors.8b01077>.
- [7] N. Joshi, T. Hayasaka, Y. Liu, H. Liu, O.N. Oliveira, L. Lin, A review on chemiresistive room temperature gas sensors based on metal oxide nanostructures, graphene and 2D transition metal dichalcogenides, *Microchim. Acta* 185 (2018), <https://doi.org/10.1007/s00604-018-2750-5>.
- [8] T. Pham, G. Li, E. Bekyarova, M.E. Itkis, A. Mulchandani, MoS<sub>2</sub>-based optoelectronic gas sensor with sub-parts-per-billion limit of NO<sub>2</sub> gas detection, *ACS Nano* 13 (2019) 3196–3205, <https://doi.org/10.1021/acsnano.8b08778>.
- [9] P. Bhattacharyya, Fabrication strategies and measurement techniques for performance improvement of graphene/graphene derivative based FET gas sensor devices: a review, *IEEE Sens. J.* 21 (2021) 10231–10240, <https://doi.org/10.1109/JSEN.2021.3060463>.
- [10] T. Han, A. Nag, S. Chandra Mukhopadhyay, Y. Xu, Carbon nanotubes and its gas-sensing applications: a review, *Sens. Actuators A Phys.* 291 (2019) 107–143, <https://doi.org/10.1016/j.sna.2019.03.053>.
- [11] Y.C. Wong, B.C. Ang, A.S.M.A. Haseeb, A. Aqilah Baharuddin, Y.H. Wong, Conducting polymers as chemiresistive gas sensing materials: a review, *J. Electrochem. Soc.* 167 (2020), <https://doi.org/10.1149/2.0032003JES>.

- [12] D.H. Ho, Y.Y. Choi, S.B. Jo, J.M. Myoung, J.H. Cho, Sensing with MXenes: progress and prospects, *Adv. Mater.* 33 (2021) 2005846, <https://doi.org/10.1002/ADMA.202005846>.
- [13] M. Sai, B. Reddy, S. Kailasa, B.C.G. Marupalli, K. Sadasivuni, S. Aich, A family of 2D-MXenes: synthesis, properties, and gas sensing applications, *ACS Sens.* 7 (2022) 2132–2163, <https://doi.org/10.1021/acssensors.2c01046>.
- [14] H. Tang, L.N. Sacco, S. Vollebregt, H. Ye, X. Fan, G. Zhang, Recent advances in 2D/nanostructured metal sulfide-based gas sensors: mechanisms, applications, and perspectives, *J. Mater. Chem. A* 8 (2020) 24943–24976, <https://doi.org/10.1039/D0TA08190F>.
- [15] J. Wang, H. Shen, Y. Xia, S. Komarneni, Light-activated room-temperature gas sensors based on metal oxide nanostructures: a review on recent advances, *Ceram. Int.* (2020), <https://doi.org/10.1016/j.ceramint.2020.11.187>.
- [16] J.O. Island, A.J. Molina-Mendoza, M. Barawi, R. Biele, E. Flores, J.M. Clamagirand, J.R. Ares, C. Sanchez, H.S.J. van der Zant, R. D'Agosta, I.J. Ferrer, A. Castellanos-Gomez, Electronics and optoelectronics of quasi-1D layered transition metal trichalcogenides, *2D Mater.* 4 (2017), 022003, <https://doi.org/10.1088/2053-1583/aa6ca6>.
- [17] M.A. Stolyarov, G. Liu, M.A. Bloodgood, E. Aytan, C. Jiang, R. Samnakay, T. T. Salguero, D.L. Nika, S.L. Romyantsev, M.S. Shur, K.N. Bozhilov, A.A. Balandin, Breakdown current density in: h-BN-capped quasi-1D TaSe<sub>3</sub> metallic nanowires: prospects of interconnect applications, *Nanoscale* 8 (2016) 15774–15782, <https://doi.org/10.1039/c6nr03469a>.
- [18] A. Geremew, M.A. Bloodgood, E. Aytan, B.W.K. Woo, S.R. Corber, G. Liu, K. Bozhilov, T.T. Salguero, S. Romyantsev, M.P. Rao, A.A. Balandin, Current carrying capacity of Quasi-1D ZrTe<sub>3</sub> Van der Waals nanoribbons, *IEEE Electron Device Lett.* 39 (2018) 735–738, <https://doi.org/10.1109/LED.2018.2820140>.
- [19] F. Kargar, A. Krayev, M. Wurch, Y. Ghafouri, T. Debnath, D. Wickramaratne, T. T. Salguero, R.K. Lake, L. Bartels, A.A. Balandin, Metallic vs. semiconducting properties of quasi-one-dimensional tantalum selenide van der Waals nanoribbons, *Nanoscale* 14 (2022) 6133–6143, <https://doi.org/10.1039/d1nr07772d>.
- [20] S. Baraghani, J. Abourahma, Z. Barani, A. Mohammadzadeh, S. Sudhindra, A. Lipatov, A. Sinitskii, F. Kargar, A.A. Balandin, Printed electronic devices with inks of TiS<sub>3</sub> quasi-one-dimensional van der Waals Material, *ACS Appl. Mater. Interfaces* (2021), <https://doi.org/10.1021/acsaami.1c12948>.
- [21] A. Patra, C.S. Rout, Anisotropic quasi-one-dimensional layered transition-metal trichalcogenides: synthesis, properties and applications, *RSC Adv.* 10 (2020) 36413–36438, <https://doi.org/10.1039/d0ra07160a>.
- [22] A.A. Balandin, F. Kargar, T.T. Salguero, R.K. Lake, One-dimensional van der Waals quantum materials, *Mater. Today* 55 (2022) 74–91, <https://doi.org/10.1016/J.MATOD.2022.03.015>.
- [23] Y. Sugita, T. Miyake, Y. Motome, Electronic band structure of 4d and 5d transition metal trichalcogenides, *Phys. B Condens. Matter* 536 (2018) 48–50, <https://doi.org/10.1016/J.PHYSB.2017.10.126>.
- [24] J. Dai, M. Li, X.C. Zeng, Group IVB transition metal trichalcogenides: a new class of 2D layered materials beyond graphene, *Wiley Interdiscip. Rev. Comput. Mol. Sci.* 6 (2016) 211–222, <https://doi.org/10.1002/WCMS.1243>.
- [25] A. Patel, C. Limberkar, K. Patel, S. Bhakhar, K.D. Patel, G.K. Solanki, V.M. Pathak, Low temperature anisotropic photoresponse study of bulk ZrS<sub>3</sub> single crystal, *Sens. Actuators A Phys.* 331 (2021), 112969, <https://doi.org/10.1016/J.SNA.2021.112969>.
- [26] N. Tripathi, V. Pavelyev, P. Sharma, S. Kumar, A. Rymzhina, P. Mishra, Review of titanium trisulfide (TiS<sub>3</sub>): a novel material for next generation electronic and optical devices, *Mater. Sci. Semicond. Process.* 127 (2021), 105699, <https://doi.org/10.1016/J.MSSP.2021.105699>.
- [27] J. Guo, J. Tao, Z. Zhang, L. Fei, D. Li, J. Jadwiszczak, X. Wang, Y. Guo, X. Liao, Y. Zhou, Controllable thermal oxidation and photoluminescence enhancement in quasi-1D van der Waals ZrS<sub>3</sub> flakes, *ACS Appl. Electron. Mater.* 2 (2020) 3756–3764, [https://doi.org/10.1021/ACSAELM.0C00788/ASSET/IMAGES/LARGE/EL0C00788\\_0007.JPEG](https://doi.org/10.1021/ACSAELM.0C00788/ASSET/IMAGES/LARGE/EL0C00788_0007.JPEG).
- [28] Y. Jin, X. Li, J. Yang, Single layer of MX<sub>3</sub> (M = Ti, Zr; X = S, Se, Te): a new platform for nano-electronics and optics, *Phys. Chem. Chem. Phys.* 17 (2015) 18665, <https://doi.org/10.1039/c5cp02813b>.
- [29] A. Patel, K. Patel, C. Limberkar, K.D. Patel, G.K. Solanki, V.M. Pathak, Wavelength dependent anisotropic photosensing activity of zirconium trisulfide crystal, *J. Mater. Sci. Mater. Electron.* 33 (2021) 8417–8425, <https://doi.org/10.1007/S10854-021-06312-8>.
- [30] S.J. Gilbert, H. Yi, J.S. Chen, A.J. Yost, A. Dhingra, J. Abourahma, A. Lipatov, J. Avila, T. Komesu, A. Sinitskii, M.C. Asensio, P.A. Dowben, Effect of band symmetry on photocurrent production in quasi-one-dimensional transition-metal trichalcogenides, *ACS Appl. Mater. Interfaces* 12 (2020) 40525–40531, [https://doi.org/10.1021/ACSAMI.0C11892/ASSET/IMAGES/LARGE/AM0C11892\\_0005.JPEG](https://doi.org/10.1021/ACSAMI.0C11892/ASSET/IMAGES/LARGE/AM0C11892_0005.JPEG).
- [31] D.S. Muratov, V.O. Vanyushin, N.S. Vorobeva, P. Jukova, A. Lipatov, E. A. Kolesnikov, D. Karpenkov, D.V. Kuznetsov, A. Sinitskii, Synthesis and exfoliation of quasi-1D (Zr,Ti)S<sub>3</sub> solid solutions for device measurements, *J. Alloy. Compd.* 815 (2020), 152316, <https://doi.org/10.1016/J.JALLCOM.2019.152316>.
- [32] Y.R. Tao, X.C. Wu, W.W. Xiong, Flexible visible-light photodetectors with broad photoresponse based on ZrS<sub>3</sub> nanobelt films, *Small* 10 (2014) 4905–4911, <https://doi.org/10.1002/smll.201401376>.
- [33] Y.R. Tao, J.J. Wu, X.C. Wu, Enhanced ultraviolet-visible light responses of phototransistors based on single and a few ZrS<sub>3</sub> nanobelts, *Nanoscale* 7 (2015) 14292–14298, <https://doi.org/10.1039/c5nr03589a>.
- [34] C.C. Mayorga-Martinez, Z. Sofer, J. Luxa, S.těpán Huber, D. Sedmidubský, P. Brázda, P. Lukáš, M. Mikulics, P. Lazar, R. Medlín, M. Pumera, TaS<sub>3</sub> nanofibers: layered trichalcogenide for high-performance electronic and sensing devices, *ACS Nano* 12 (2018) 464–473, <https://doi.org/10.1021/acsnano.7b06853>.
- [35] N. Rafiefard, A. Irají Zad, A. Esfandiari, P. Sasanpour, S. Fardindoost, Y. Zou, S. J. Haigh, S. Hossein, H. Shokouh, A graphene/TiS<sub>3</sub> heterojunction for resistive sensing of polar vapors at room temperature, *Microchim. Acta* 187 (2020) 117, <https://doi.org/10.1007/s00604-019-4097-y>.
- [36] Z. Barani, F. Kargar, Y. Ghafouri, S. Ghosh, K. Godziszewski, S. Baraghani, Y. Yashchishyn, G. Cywiński, S. Romyantsev, T.T. Salguero, A.A. Balandin, Electrically insulating flexible films with Quasi-1D van der Waals fillers as efficient electromagnetic shields in the GHz and Sub-THz frequency bands, *Adv. Mater.* 33 (2021) 1–9, <https://doi.org/10.1002/adma.202007286>.
- [37] G.F. Fine, L.M. Cavanagh, A. Afonja, R. Binions, Metal oxide semi-conductor gas sensors in environmental monitoring, *Sensors* 10 (2010) 5469–5502, <https://doi.org/10.3390/s100605469>.
- [38] P.T. Moseley, Progress in the development of semiconducting metal oxide gas sensors: a review, *Meas. Sci. Technol.* 28 (2017), <https://doi.org/10.1088/1361-6501/aa7443>.
- [39] M. Khatib, H. Haick, Sensors for volatile organic compounds, *ACS Nano* (2022), <https://doi.org/10.1021/acsnano.1c10827>.
- [40] C. Jaeschke, J. Glöckler, O. El Azizi, O. Gonzalez, M. Padilla, J. Mitrovics, B. Mizaikoff, An innovative modular eNose system based on a unique combination of analog and digital metal oxide sensors, *ACS Sens.* 4 (2019) 2277–2281, <https://doi.org/10.1021/acssensors.9b01244>.
- [41] H. Fang, W. Hu, Photogating in low dimensional photodetectors, *Adv. Sci.* 4 (2017), <https://doi.org/10.1002/advs.201700323>.
- [42] M.M. Furchi, D.K. Polyushkin, A. Pospischil, T. Mueller, Mechanisms of photoconductivity in atomically thin MoS<sub>2</sub>, *Nano Lett.* 14 (2014) 6165–6170, <https://doi.org/10.1021/nl502339q>.
- [43] H. Tabata, H. Matsuyama, T. Goto, O. Kubo, M. Katayama, Visible-light-activated response originating from carrier-mobility modulation of NO<sub>2</sub> gas sensors based on MoS<sub>2</sub> monolayers, *ACS Nano* 15 (2021) 2542–2553, <https://doi.org/10.1021/acsnano.0c06996>.
- [44] B. Cui, Y. Xing, J. Han, W. Lv, W. Lv, T. Lei, Y. Zhang, H. Ma, Z. Zeng, B. Zhang, Negative photoconductivity in low-dimensional materials, *Chin. Phys. B* 30 (2021) 28507, <https://doi.org/10.1088/1674-1056/abc4f1>.
- [45] A. Bag, D. Bin Moon, K.H. Park, C.Y. Cho, N.E. Lee, Room-temperature-operated fast and reversible vertical-heterostructure-diode gas sensor composed of reduced graphene oxide and AlGaIn/GaN, *Sens. Actuators B Chem.* 296 (2019), 126684, <https://doi.org/10.1016/j.snb.2019.126684>.